Exp Fluids (2008) 44:691–703
DOI 10.1007/s00348-007-0427-7

RESEARCH ARTICLE

Scale effects in subaerial landslide generated impulse waves

Valentin Heller · Willi H. Hager · Hans-Erwin Minor

Received: 25 January 2007 / Revised: 2 November 2007 / Accepted: 6 November 2007 / Published online: 4 December 2007

Abstract Hydraulic scale modelling involves scale effects. The limiting criteria for scale models of subaerial landslide generated impulse waves including solid, air, and water are discussed both based on a literature review and based on detailed two-dimensional experimentation. Seven scale series based on the Froude similitude were conducted involving the intermediate-water wave spectrum. Scale effects were primarily attributed to the impact crater formation, the air entrainment and detrainment, and the turbulent boundary layer as a function of surface tension and fluid viscosity. These effects reduce the relative wave amplitude and the wave attenuation as compared with reference experiments. Wave amplitude attenuation was found to be more than 70 times larger than predicted with the standard wave theory. Limitations for plane impulse wave generation on the basis of the present research are given by which scale effects can be avoided.

List of symbols

a	wave amplitude (L)
$a_{x'}$	wave amplitude at distance x' from CWG_1 (L)
A	relative wave amplitude (−)
A_{1d}	relative amplitude difference at CWG_1 (%)
A_{1dtot}	total relative amplitude difference (%)
A_{1dZ}	relative amplitude difference according to Zweifel et al. (2006) (%)
A_{1ref}	relative reference amplitude at CWG_1 (−)
b	channel width (L)
c	wave celerity (LT^{-1})
C	Cauchy number (−)
d_g	grain diameter (L)
D	relative slide density (−)
D_g	relative grain diameter (−)
F	slide Froude number (−)
g	gravitational acceleration (LT^{-2})
h	still water depth (L)
H	wave height (L)
j	number of governing dimensionless quantities (−)
L	wavelength (L)
m	number of governing independent parameters on impulse wave generation (–)
m_s	slide mass (M)
M	relative slide mass (−)
n	bulk slide porosity (%)
o	number of fundamental units (−)
p_A	box acceleration air pressure ($ML^{-1}T^{-2}$)
R	Reynolds number (−)
s	slide thickness (L)
S	relative slide thickness (−)
t	time (T)
T	wave period (T)
T_r	relative time (−)
Te	water temperature (°C)
V	relative slide volume (−)
V_s	slide impact velocity (LT^{-1})
$\forall_s$	slide volume identical to box volume (L^3)
W	Weber number (−)
x	streamwise coordinate (L)
x'	distance from CWG_1 (L)
X	relative streamwise distance (−)
Y_P	relative primary wave height (−)
z	vertical coordinate (L)
α	slide impact angle (°)

V. Heller (✉) · W. H. Hager · H.-E. Minor
Laboratory of Hydraulics, Hydrology and Glaciology (VAW), ETH Zurich, 8092 Zurich, Switzerland
e-mail: heller@vaw.baug.ethz.ch

β average wave amplitude attenuation (%)
δ dynamic bed friction angle (°)
Δ time increment (T)
$\Delta x'$ spacing between CWG_1 and CWG_7 (L)
ΔX relative spacing between CWG_1 and CWG_7 (−)
ϕ' internal friction angle (°)
η water surface displacement (L)
κ_w water compressibility (LT^2M^{-1})
ν_w kinematic viscosity for water (L^2T^{-1})
ρ density (ML^{-3})
σ_w surface tension for water (MT^{-2})

Subscripts
A acceleration
d difference
g grain
K Keulegan
L limit
M maximum
P primary
r relative
ref reference
s slide
tot total
w water
Z Zweifel
1 at CWG_1
3 at CWG_3
5 at CWG_5
7 at CWG_7

1 Introduction

Subaerial landslides, snow avalanches, and glacier or rock falls may generate large impulse waves in lakes or oceans, as the 1958 Lituya Bay case where a wave run-up height of 524 m was reached (Miller 1960). Scale model tests were conducted to investigate this complex multiphase phenomenon with solid, air, and water involved (Fritz et al. 2001). Given the large flow field that had to be modelled, the scale was 1:675. The question then applies whether the major effects of such a process are retained in a hydraulic model. The following addresses the limiting hydraulic conditions relative to plane impulse waves, based on the hydraulic similitude and on a detailed laboratory investigation, in which families of scale models were carefully investigated in terms of surface tension and fluid viscosity.

The perfect similitude between a hydraulic model and its prototype requires geometric, kinematic, and dynamic similarity (Hughes 1993; Heller 2007b). For *geometrical* similarity, all ratios of the corresponding linear dimensions (e.g. length) must be identical between the model and the prototype; the *kinematic* similarity applies to all components of the vectorial motions for all particles at any time (e.g. time) involved in the flow process; in addition, the ratios of *all* vectorial forces (e.g. gravity) in the two systems must be identical for *dynamic* similarity.

The relevant forces of landslide generated impulse waves are the inertial, the gravitational, the viscous, the surface tension, and the elastic compression forces. No fluid may satisfy *all* force ratio requirements if the model is smaller (or larger) than the prototype. An important task in scale model design is to identify the important force ratio and to provide justification for neglecting the others (Hudson et al. 1979). The most relevant force ratio in free surface flows is the square root of the inertial to the gravity forces, i.e. the Froude number. If a process is governed by the Froude similitude, then (1) the Reynolds criterion including viscous forces, (2) the Weber criterion accounting for surface tension forces, and (3) the Cauchy criterion as the ratio of inertial to elastic forces are neglected. This paper aims to discuss the limiting conditions of scale effects in subaerial landslide generated impulse waves.

Hughes (1993) proposed four methods to ascertain model similitude: (a) calibration, (b) differential equations, (c) dimensional analysis, and (d) scale families. Methods (a) and (b) are hardly applicable to subaerial landslide generated impulse waves since (a) prototype data are rare and (b) the complete set of differential equations for this three-phase phenomenon is not available. The governing parameters of a physical process are expressed in (c) as independent dimensionless parameters containing the relevant physical information. To preserve exact similitude, these must be identical in model and prototype. In method (d) experiments in models of different scales are conducted, with the model of the largest dimension serving as the reference. The latter two possibilities (c) and (d) were applied herein.

Section 2 presents a literature review of relevant impulse wave experimentation. The experimental model and the dimensional analysis are detailed in Sect. 3. In Sect. 4, the results of seven scale series are described, and discussed in Sect. 5 with respect to scale effects. The limitations for scale effects are summarized in Sect. 5.3. Conclusions resume the results of this research.

2 Literature review

2.1 Hydraulic modelling

According to Le Méhauté (1976, 1990) the Froude similitude applies to free surface flows with negligible viscous forces, e.g. prior to wave breaking or to short, highly turbulent flows such as in the wave breaking zone. The energy

dissipation process is in similitude as for hydraulic jumps, even if the fine turbulent structure is not completely retained.

Subaerial landslide generated impulse waves were experimentally investigated using a block model (Noda 1970; Kamphuis and Bowering 1972; Heinrich 1992; Walder et al. 2003; Panizzo 2004; Panizzo and De Girolamo 2005; among others) or granular material (Huber 1980; Fritz et al. 2003; Zweifel et al. 2006; Heller 2007a). Huber (1980) analysed the two- and three-dimensional wave phenomena and found the wave height attenuation to depend on the wave type and the wave height; further, relatively small waves decayed more than larger waves. Fritz et al. (2003) designed a novel pneumatic landslide acceleration mechanism to generate impact slides of which the impact velocity and the slide thickness may nearly independently be varied. Particle image velocimetry (PIV) was further applied to evaluate the 2D wave generation flow field in the wave channel. This hydraulic model was used by Zweifel et al. (2006), and Heller (2007a) to conduct the present research. Despite the existing model tests on landslide generated impulse waves, scale effects have so far not received a systematic analysis.

2.2 Slide impact zone

Wave breaking including air entrainment and turbulence generation is similar to the impulse wave generation. Miller (1972) highlighted the relevance of surface tension on wave breaking with experiments using detergent to change the surface tension of the water. Skladnev and Popov (1969) demonstrated experimentally with wave heights from 0.03 to 1.20 m that scale effects for waves higher than 0.50 m remain small in terms of wave forces on a concrete slope during the wave breaking process. Führböter (1970) discussed the energy dissipation process of breaking waves due to air entrainment. The air entrainment depends not only on the Froude and the Reynolds but in addition on the Weber number. The energy dissipation due to the air–water flow was found to be dominant as compared with viscous interactions along the bottom. Stive (1985) investigated wave breaking in two different wave flumes of dimensions (a) 233 m long, 5 m wide, and 7 m deep using a still water depth of $h = 4.19$ m, and (b) 55 m long, 1 m wide, and 1 m deep with a still water depth $h = 0.70$ m. Scale effects relative to the wave height or the time-averaged horizontal velocities were virtually absent for wave heights $0.1 < H < 1.5$ m. Experimentation of impulse waves involved until today always the Froude similitude, because the relevant forces include gravity and inertia. The application limits of such hydraulic experimentation should be carefully investigated to up-scale model results to prototype scale.

2.3 Wave attenuation

Depending on the Reynolds number, hydraulic models scaled with the Froude criterion do not correctly retain viscous effects (Hughes 1993). For sinusoidal deep-water waves with negligible boundary effects, Keulegan (1950) developed an estimate for the wave amplitude attenuation due to fluid viscosity as

$$a(t)/a(t=0) = \exp(-8\pi^2 \nu_w t/L^2) \quad (1)$$

where $a(t)$ is the attenuated positive wave amplitude at time t, L is the wavelength, and ν_w is the kinematic viscosity of water ($\nu_w = 10^{-6}$ m^2/s for 20°C; subscript w). Keulegan (1950) also presented an analytical expression for the wave amplitude damping of a solitary wave in a rectangular channel due to boundary layer existence. Assuming potential flow outside of the boundary layer the wave amplitude attenuation results from equating the boundary layer dissipation with the rate of energy decay of a solitary wave as

$$(a_{x'}/h)^{-1/4} - (a_1/h)^{-1/4} = x'/[12h][1+2h/b][\nu_w^2/(gh^3)]^{1/4}. \quad (2)$$

In Eq. 2, a_1 is the reference amplitude at the first measuring point $x' = 0$, i.e. at the first capacitance wave gauge (CWG_1; subscript 1) of the VAW model, $a_{x'}$ is the wave amplitude attenuation at distance x' from CWG_1, b is channel width, and g the gravitational acceleration. Consequently, the amplitude damping of a solitary wave decreases as the channel width b increases and the kinematic viscosity ν_w decreases. Further analytical expressions for the wave attenuation due to fluid viscosity were presented by Biesel (1949) for sinusoidal, by Iwasa (1959) for solitary, by De St Q Isaacson (1976) for cnoidal, and by Miles (1976) for cnoidal and solitary waves. Experimental data for wave attenuation were presented, amongst others, by Ippen and Kulin (1957) and Treloar and Brebner (1970). Ippen and Kulin (1957) generated solitary waves in a wave channel of width $b = 0.42$ m, 9.75 m length, and still water depths from $h = 0.06$ to 0.12 m on hydraulic smooth and rough bottoms. The damping coefficient of their smooth bed data was 20–30% larger than from Eq. 2. Treloar and Brebner (1970) separated the influences of channel sidewalls and bottom on the wave height attenuation with two identically flumes of different widths $b = 0.61$ and 0.91 m for a range of deep-water to cnoidal waves. Their experiments were combined with an analytical approach to

provide a semi-empirical equation for wave height damping.

On the basis of a wavelet transform analysis Panizzo et al. (2002) demonstrated that landslide generated impulse waves may be interpreted as a superposition of several wave components of different frequencies. According to the *linear* dispersion relation (e.g. Dean and Dalrymple 2004), a shallow-water wave is non-dispersive since its celerity depends only on the still water depth h. Intermediate and deep-water waves are however dispersive, i.e. the wave components separate, since their celerity depend on the wave period T. Whereas mainly the fluid viscosity v_w is relevant for wave damping in shallow-water, the frequency dispersion has an additional effect on the wave amplitude attenuation in intermediate and deep-water. The same phenomenon of frequency dispersion applies also for *nonlinear* waves, such as the solitary wave.

Surface tension has a major influence on the wave celerity (Huber 1976). Le Méhauté (1990) and Hughes (1993) demonstrated that this effect is relevant for still water depths $h < 0.02$ m or wave periods of $T < 0.35$ s for pure water waves, i.e. much smaller than in this study. Surface tension affects in addition the crater formation during the wave generation phase of impulse waves, as shown below.

According to Hughes (1993) compressibility effects in coastal engineering are small because water can be considered as incompressible. Forces on a structure caused by the compression of air trapped in wave breakers are an exception. Abelson (1970) measured the pressure in a cavity behind a projectile impacting a water body with angles of 90, 60, and 45°. For impact velocities of up to 10.4 m/s, the pressure conforms with atmospheric pressure whereas the pressure data decrease linearly to half of it at 80 m/s. Compressibility effects are not appropriately reproduced in this study as compared with prototypes since the slide impact velocity is smaller than 10.4 m/s. Scale effects originating from the density difference between fresh and sea water as discussed by Le Méhauté (1990) are not considered subsequently.

3 Physical model

3.1 Wave channel

The present research includes a total of 18 individual experiments within the seven scale series S1 to S7 to analyse scale effects, as presented in Sect. 4. These were carried out in a rectangular prismatic water wave channel, 11 m long, 0.5 m wide, and 1 m deep as shown in Fig. 1 (Fritz 2002). A splash protection avoided the wetting of the surroundings and a wave absorber at the channel end reduced wave reflection. The 3 m long ramp had a slide impact angle of $\alpha = 45°$. The landslide box was accelerated with up to 4.5 bar air pressure using a pneumatic acceleration mechanism (Fritz and Moser 2003). This pneumatic landslide generator allowed to vary independently all important parameters for the impulse wave generation under a high test repetition accuracy (Heller 2007a). When

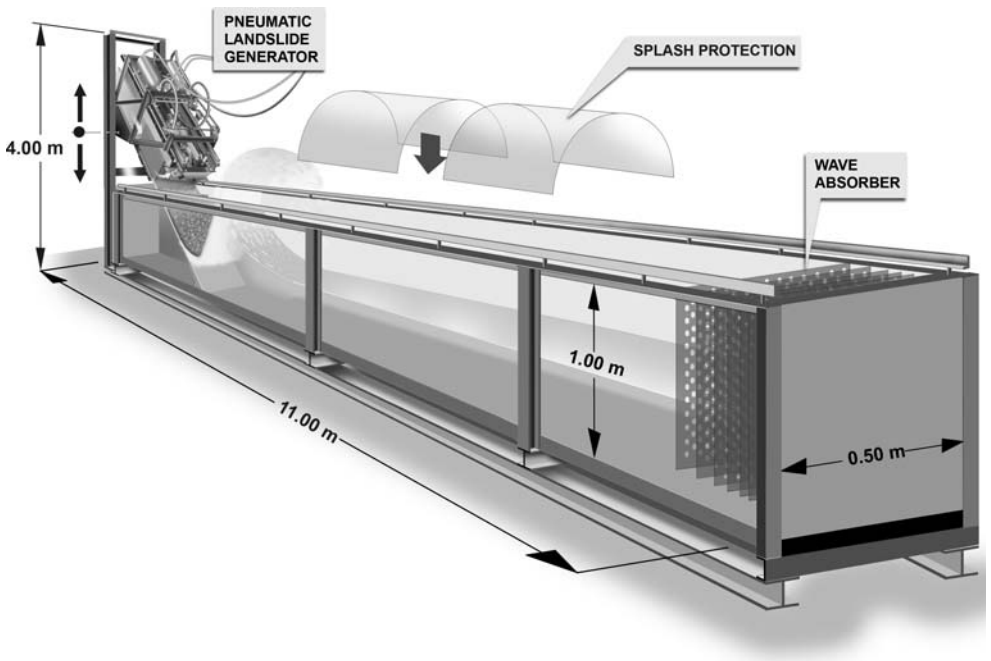

Fig. 1 Wave channel with main dimensions, pneumatic landslide generator, splash protection, and wave absorber (Fritz 2002)

Table 1 Granular materials properties

Granulate	d_g (mm)	ρ_g (kg/m^3)	ρ_s (kg/m^3)	n (%)	δ (°)	ϕ' (°)
Fig. 2a	2	2,372	1,442	39	27	32
Fig. 2b	4	2,745	1,592	42	24	34
Fig. 2c	8	2,429	1,338	45	21	34

the landslide box had reached its maximum velocity, the front flap opened and the slide material accelerated further down the hill slope ramp.

Slide (subscript s) impact velocities in the range of $3.5 \leq V_s \leq 6.9$ m/s resulted from box acceleration. For the tests with a scale of 1:4 as compared with the reference experiment the slide impact velocity V_s should be half of the reference velocity according to the Froude similitude. This was impossible for the velocity range previously stated. Therefore, the flap was normally opened at the box end position without prior acceleration for the tests of small scales such that the slide impact velocity V_s resulted only from gravity. Inner box lengths were 0.6, 0.3, and 0.15 m, with corresponding inner box heights of 0.236, 0.118, and 0.059 m. The inner box width was 0.472 m, resulting in box volumes of $\forall_s = 0.0668$, 0.0167, and 0.0042 m^3. The flume front sidewall was of glass, whereas the back sidewall consisted of a continuous steel plate. The channel bottom was made of steel in the slide impact zone and was glassed further downstream. For the scale series S6 and S7, the original channel width of $b = 0.500$ m was reduced to 0.250 and to 0.125 m, respectively, using a wooden wall coated with a smooth black adhesive film on the front side to reduce boundary friction. One half or alternatively one quarter of the slide volume $\forall_s$ generated the impulse wave in the observational zone. The exact mass of slide material was determined after each test.

All measurements were recorded along the wave channel axis. Two laser distance sensors (LDS) measured the granular slide profiles with a frequency of 100 Hz. The static water level calibration required at least 1 h. Therefore, the water surface was always contaminated in terms of Miller (1972) or Miles (1976), which may affect the surface tension. The still water depth h was controlled with a point gage of ±0.5 mm accuracy. The wave features in the propagation zone were determined using seven capacitance wave gages with a sampling frequency of 500 Hz and a constant spacing of 1, 0.5, or 0.25 m among each other, respectively. The CWGs were installed from (1/3)h over the channel bottom and they measured the wave crest height below the breaking limit with an accuracy of ±1.5 mm (Fritz 2002). The water temperature Te was between 21 and 27°C (±0.5°C).

The landslides were modelled with three artificial granular materials of grain (subscript g) diameter $d_g = 8$, 4, and 2 mm, a granular density $2{,}372 \leq \rho_g \leq 2{,}745$ kg/m^3, a bulk slide density $1{,}338 \leq \rho_s \leq 1{,}592$ kg/m^3, a bulk slide porosity $39 \leq n \leq 45\%$, a dynamic bed friction angle $21 \leq \delta \leq 27°$, and an internal friction angle $32 \leq \phi' \leq 34°$ (Table 1, Fig. 2). The grains were cylindrical with a ratio of grain diameter d_g to grain height of about 2.5. It consisted of 87% barium-sulphate ($BaSO_4$) compounded with 13% polypropylene (PP) to satisfy density and hardness requirements. The slide material was normally damp prior to a test and only the smallest grains without pneumatic acceleration were dry to prevent that a considerable portion of the material remained in the box.

3.2 Dimensional analysis

A dimensional analysis was conducted to determine the governing dimensionless parameters on impulse wave generation and propagation (Buckingham 1914). Figure 3 shows a definition sketch with the seven governing independent parameters, namely, the still water depth h (=0.075–0.600 m), the slide impact velocity V_s (=2.033–6.040 m/s), the slide thickness s (=0.017–0.166 m), the bulk slide volume $\forall_s$ (=0.004–0.067 m^3), the bulk slide density ρ_s (=1,338–1,592 kg/m^3), the grain diameter d_g (=2–8 mm), and the slide impact angle α (=45°). Further, the water density ρ_w (kg/m^3), the gravitational acceleration

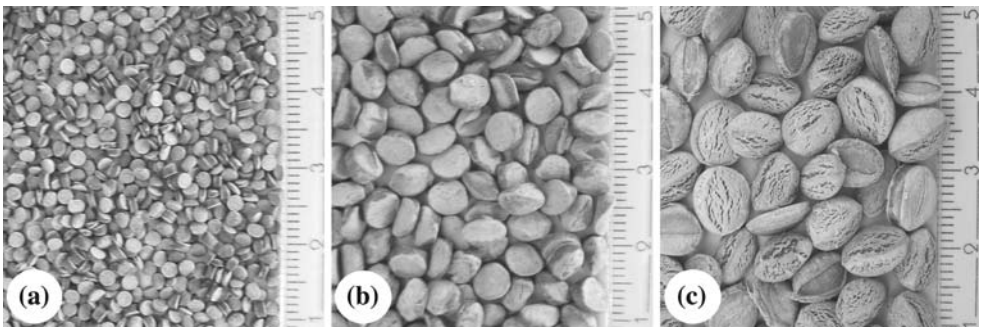

Fig. 2 Cylindrical granular slide material (PP–$BaSO_4$): grain diameter d_g = (**a**) 2 mm, (**b**) 4 mm, and (**c**) 8 mm

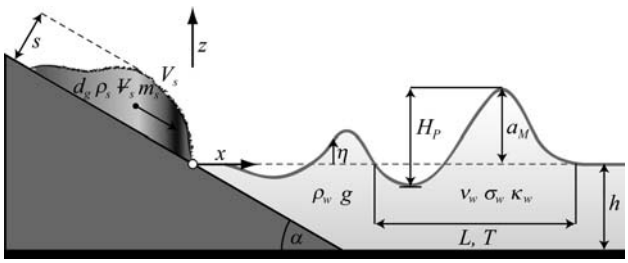

Fig. 3 Definition plot with the slide (*left*), the water body (*right*), and the impulse wave parameters

g (m/s^2), the distance x (m) from the intersection of still water depth and the hill slope ramp, and the time t (s) influence the maximum (subscript M) wave amplitude a_M, the primary (subscript P) wave height H_P, the water surface displacement η, the wave period T, or the wavelength L. The vertical coordinate z and the slide mass $m_s = \rho_s \forbar{V}_s$ were not included in the dimensional analysis. An approach based on the Froude similitude excludes the effects of the

$$\text{Reynolds number, } \mathrm{R} = g^{1/2}h^{3/2}/\nu_w, \tag{3}$$

$$\text{Weber number, } \mathrm{W} = \rho_w g h^2/\sigma_w, \tag{4}$$

$$\text{Cauchy number, } \mathrm{C} = \kappa_w \rho_w V_s^2. \tag{5}$$

These involve the shallow-water wave celerity $(gh)^{1/2}$, the kinematic fluid viscosity ν_w (m^2/s), the surface tension σ_w (N/m), and the fluid compressibility κ_w (m^2/N). The independent parameters have the three fundamental units (m, kg, t); therefore, the three fundamental scalings h, g, and ρ_w were retained, resulting in $j = m - o = 11 - 3 = 8$ dimensionless quantities with $m = 11$ as the involved governing independent parameters and the fundamental units $o = 3$ (Buckingham 1914). These are the slide Froude number $\mathrm{F} = V_s/(gh)^{1/2}$, the relative slide thickness $S = s/h$, the relative slide volume $V = \forbar{V}_s/(bh^2)$, the relative slide density $D = \rho_s/\rho_w$, the relative streamwise distance $X = x/h$, the slide impact angle α, the relative grain diameter $D_g = d_g/h$, and the relative (subscript r) time $T_r = t(g/h)^{1/2}$. The slide impact angle α was kept constant in the present study. Zweifel et al. (2006) showed that the relative slide volume V and the slide density D can be combined into the relative slide mass $M = VD = m_s/(\rho_w b h^2)$. Heller (2007a) demonstrated that the effect of the relative grain diameter $D_g = d_g/h$ on the primary impulse waves is small. Consequently, to evaluate scale effects using scale series, the parameters F, S, M, X, and T_r were kept constant within a test series (Table 2).

4 Results

4.1 Impact zone

A photo sequence of test S7/1 (Table 2) for F = 2.44, $S = 0.27$, and $M = 1.22$ involving negligible scale effects (see below) is shown in Fig. 4 for a time step of $\Delta t = 0.333$ s. Figure 4a relates to the initial conditions

Table 2 Basic parameters of scale series S1 to S7 with boundary conditions, slide Froude number F, relative slide thickness S, and relative slide mass M

Run	H (m)	p_A (bar)	Te (°C)	b (m)	$\forbar{V}_s$ (m^3)	x_1 (m)	$\Delta x'$ (m)	d_g (mm)	V_s (m/s)	s (m)	m_s (kg)	F (−)	S (−)	M (−)
S1/1	0.600	0.0	22	0.500	0.067	1.730	6.00	8	4.192	0.132	96.63	1.73	0.22	0.54
S1/2	0.300	0.0	22	0.500	0.017	0.865	3.00	4	3.009	0.058	24.98	1.75	0.19	0.56
S1/3	0.150	0.0	22.5	0.500	0.004	0.433	1.50	2	2.033	0.023	6.51	1.68	0.15	0.58
S2/1	0.300	0.0	22	0.500	0.017	0.865	3.00	8	3.131	0.069	24.28	1.83	0.23	0.54
S2/2	0.150	0.0	22.5	0.500	0.004	0.433	1.50	4	2.133	0.024	7.02	1.76	0.16	0.62
S3/1	0.200	4.2	27	0.500	0.017	0.765	3.00	4	5.945	0.083	26.27	4.25	0.42	1.31
S3/2	0.100	2.0	23	0.500	0.004	0.383	1.50	2	4.029	0.042	6.59	4.07	0.42	1.32
S4/1	0.400	1.5	23	0.500	0.067	1.530	6.00	8	4.889	0.166	95.69	2.47	0.42	1.20
S4/2	0.200	0.0	25.5	0.500	0.017	0.765	3.00	4	3.592	0.049	25.38	2.57	0.25	1.27
S4/3	0.100	0.0	25	0.500	0.004	0.383	1.50	2	2.511	0.017	6.28	2.54	0.17	1.26
S5/1	0.300	1.5	24.5	0.500	0.067	1.430	6.00	8	5.014	0.160	97.15	2.92	0.53	2.16
S5/2	0.150	0.0	26	0.500	0.017	0.715	3.00	4	3.676	0.043	25.25	3.03	0.29	2.24
S5/3	0.075	0.0	26.5	0.500	0.004	0.358	1.50	2	2.561	0.017	6.27	2.99	0.23	2.23
S6/1	0.300	4.5	21	0.250	0.017	0.865	3.00	4	6.040	0.063	12.71	3.52	0.21	0.56
S6/2	0.150	2.0	22.5	0.125	0.004	0.433	1.50	2	4.216	0.039	1.53	3.48	0.26	0.54
S7/1	0.400	1.5	22	0.500	0.067	1.530	6.00	8	4.831	0.101	97.48	2.44	0.25	1.22
S7/2	0.200	0.0	22	0.250	0.017	0.765	3.00	4	3.693	0.051	13.65	2.64	0.25	1.36
S7/3	0.100	0.0	22.5	0.125	0.004	0.383	1.50	2	2.396	0.020	1.58	2.42	0.20	1.27

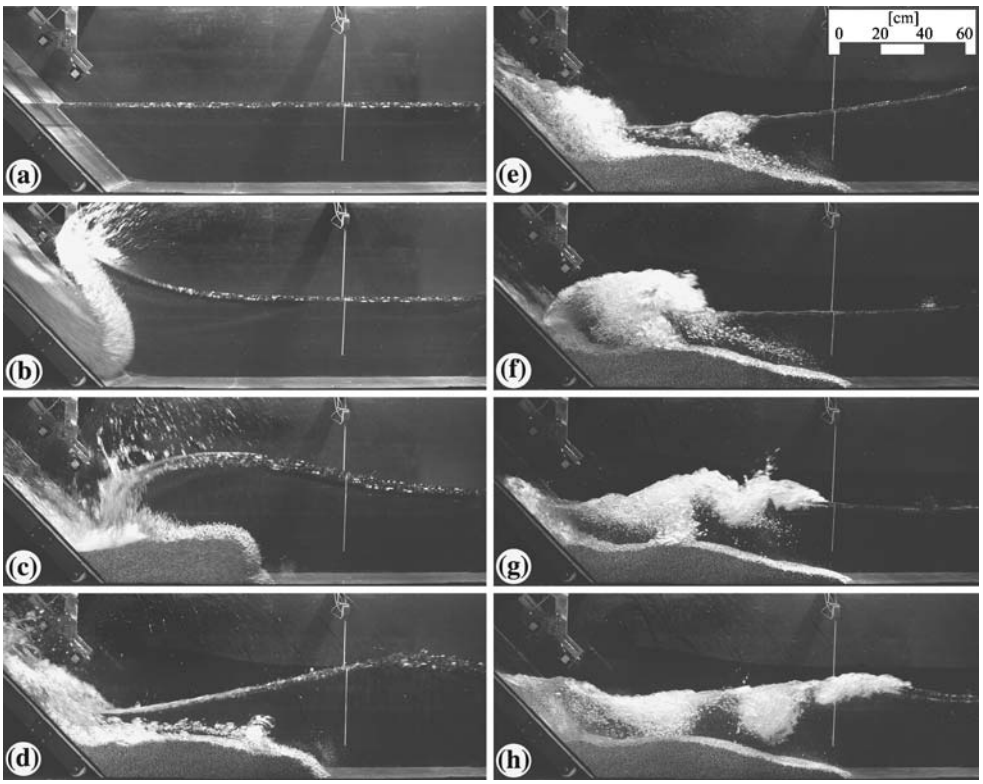

Fig. 4 Photo sequence of granular slide impact and impulse wave generation of Run S7/1 with negligible scale effects for F = 2.44, S = 0.27, and M = 1.22, time increment Δt = 0.333 s

with the still water depth h = 0.400 m, the two LDSs to the left and the first capacitance wave gage CWG_1 to the right. The granular material impacts the water body in Fig. 4b with a splash development and the impact crater between the slide surface and the water body. The water is lifted almost vertically because of the slide displacement. The air cavity collapses in Fig. 4c resulting in the primary impulse wave of maximum wave amplitude at CWG_1 between Fig. 4c and d. The air entrained along the slide surface and contained in the slide pores escapes mainly onto the hill-slope ramp during wave run-up, as may be observed from Fig. 4d, e. The backflow from the ramp generates a secondary wave as is seen from Fig. 4d–h entraining additional air and producing turbulence due to wave breaking. This bore type wave reaches CWG_1 in Fig. 4g. In Fig. 4e the slide rests at its terminal position. These photos define the temporal advances of both the water and the slide material surfaces. Because of the local phenomenon, fluid viscosity plays a small role in the wave generation phase. For bore type impulse waves, the leading wave front resembles a hydraulic jump for which scale effects are known to be small, except for approach flow depths smaller than some centimetres (Hager and Bremen 1989).

4.2 Experimental programme

A total number of 18 experiments allocated to seven scale series S1 to S7 were conducted (Table 2). The first experiment within a scale series was considered the reference test. Table 2 includes next to h, b, and Te the slide parameters ~~V_s~~, d_g, V_s, s, and m_s as defined in Fig. 3 resulting in slide Froude numbers $1.68 \leq F \leq 4.25$, relative slide thicknesses $0.15 \leq S \leq 0.53$, and relative slide masses $0.54 \leq M \leq 2.24$. In the scale series S4, S5, and S7 the acceleration (subscript A) air pressure p_A on the slide box varied from 0 (i.e. the flap opens at the box end position without acceleration) to 1.5 bar resulting in a certain slide Froude number F within a scale series. For accelerated experiments the box end position had to be much closer to the still water surface to result in the appropriate slide impact velocity V_s. As a consequence, the slide travel distance was much smaller than with p_A = 0 bar resulting in a larger slide thickness s. It was therefore difficult to simultaneously reach a constant slide thickness S *and* a slide Froude number F within a scale series. In contrast, the control of the relative slide mass M consisting of the static parameters m_s, b, h, ρ_w posed few problems. Table 2 includes also the distances x_1 of CWG_1 from the

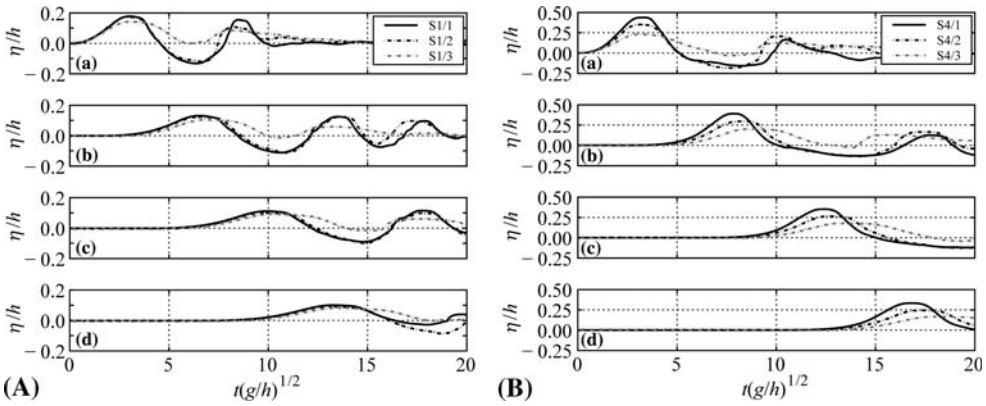

Fig. 5 Relative wave profiles $\eta/h[t(g/h)^{1/2}]$ for scale series (**A**) S1 and (**B**) S4 at locations (**a**) CWG_1, (**b**) CWG_3, (**c**) CWG_5, and (**d**) CWG_7

origin and the spacing $\Delta x'$ between CWG_1 and CWG_7 (subscript 7).

4.3 Wave propagation

The wave profiles of the test series S1 and S4 are shown in Figs. 5A and B, respectively. The relative wave amplitude η/h is plotted versus the relative time $T_r = t(g/h)^{1/2}$. The wave profiles recorded at (a) CWG_1, (b) CWG_3 (subscript 3), (c) CWG_5 (subscript 5), and (d) CWG_7 are shown from top to the bottom. The parameter T_r was adjusted between the different tests within a scale series to the first increase of the relative amplitude η/h at CWG_1. The reference tests S1/1 and S4/1 are shown as a full black line, whereas the dash-dotted black and grey lines refer to the tests of (1/2) and (1/4) scale, respectively (Table 2). Test S1/2 follows the primary wave of S1/1 whereas the wave train differs. The relative amplitude of S1/3 with $h = 0.150$ m is different from test S1/1. Note that test S1/1 in Fig. 5A, d is influenced by wave reflection from the wave absorber for $T_r > 15$. In Fig. 5B the relative amplitudes of both S4/2 and S4/3 differ from S4/1. Besides scale effects, the slide Froude number F, the relative slide thickness S, and the relative slide mass M were difficult to keep *exactly* constant within the scale series, as previously explained (Table 2).

Table 3 is a sequel of Table 2 with additional measured and computed impulse wave quantities. The relative amplitude $A_1 = a_1/h$ measured at CWG_1 for the primary wave of the reference (subscript *ref*) tests is always larger than of the downscaled tests, expressed with the relative amplitude difference (subscript *d*) $A_{1d} = 100(A_1/A_{1ref}-1)$.

Table 3 Continuation of Table 2 with measured and calculated impulse wave properties

Run	A_1 (−)	A_7 (−)	$\Delta X'$ (−)	β (%)	β_K (%)	A_{1d} (%)	A_{1dZ} (%)	A_{1dtot} (%)	c_1 (m/s)	T_1 (s)	L_1 (m)	L_1/h (−)	R (−)	W (−)
S1/1	0.178	0.100	10.0	43.8	0.60	0.0	0.0	0.0	2.39	1.78	4.26	7.10	1,503,402	48,111
S1/2	0.174	0.091	10.0	47.7	0.65	−2.25	4.0	1.8	1.56	1.18	1.84	6.14	531,533	12,027
S1/3	0.143	0.083	10.0	42.0	0.75	−19.7	17.5	−2.22	1.07	0.65	0.70	4.66	189,986	3,006
S2/1	0.185	0.101	10.0	45.4	0.66	0.0	0.0	0.0	1.57	1.22	1.91	6.38	531,533	12,027
S2/2	0.179	0.099	10.0	44.7	0.79	−3.24	16.8	13.6	1.06	0.85	0.90	5.97	189,986	3,006
S3/1	1.050	0.808	15.0	23.0	1.58	0.0	0.0	0.0	2.00	1.66	3.32	16.58	324,532	5,345
S3/2	0.659	0.514	15.0	22.0	1.93	−37.24	3.5	−33.74	1.71	1.05	1.80	18.04	104,561	1,336
S4/1	0.437	0.332	15.0	24.0	1.15	0.0	0.0	0.0	2.17	1.83	3.99	9.97	836,495	21,382
S4/2	0.352	0.244	15.0	30.7	1.23	−19.52	18.8	−0.75	1.43	1.23	1.75	8.76	313,103	5,345
S4/3	0.232	0.166	15.0	28.4	1.45	−46.99	34.0	−13.04	0.95	0.94	0.89	8.86	109,414	1,336
S5/1	0.631	0.565	20.0	10.5	1.72	0.0	0.0	0.0	2.03	1.81	3.68	12.26	562,014	12,027
S5/2	0.485	0.407	20.0	16.1	1.94	−23.09	23.7	0.6	1.32	1.27	1.67	11.16	205,782	3,006
S5/3	0.403	0.331	20.0	17.9	2.50	−36.19	33.3	−2.9	0.76	0.63	0.48	6.38	73,629	751
S6/1	0.844	0.395	10.0	53.2	1.49	0.0	0.0	0.0	1.76	1.63	2.87	9.57	520,246	12,027
S6/2	0.444	0.226	10.0	49.1	2.09	−47.39	−8.24	−55.63	1.25	0.94	1.18	7.85	189,986	3,006
S7/1	0.378	0.294	15.0	22.2	1.12	0.0	0.0	0.0	2.17	1.85	4.01	10.03	818,348	21,382
S7/2	0.317	0.212	15.0	33.1	1.79	−16.08	−11.7	−27.78	1.41	1.21	1.71	8.56	289,329	5,345
S7/3	0.213	0.138	15.0	35.2	2.70	−43.61	11.8	−31.81	1.02	0.76	0.78	7.77	103,415	1,336

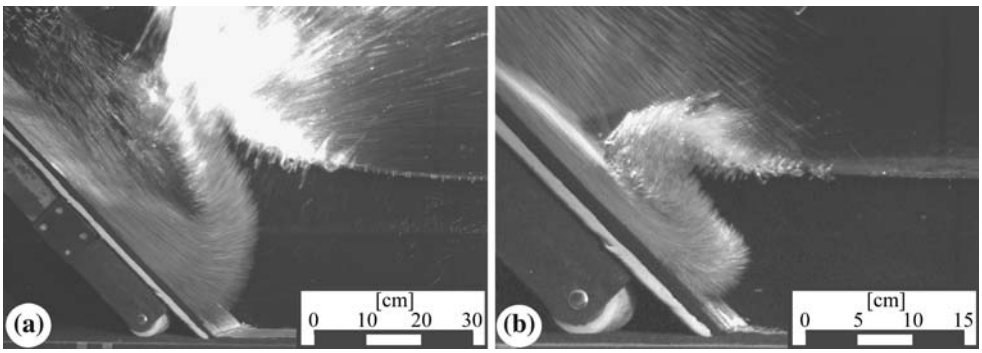

Fig. 6 Impact crater formation for (**a**) test S6/1, and (**b**) test S6/2 increased by a factor of 2

The relative amplitude $A_7 = a_7/h$ at CWG_7 was measured at the relative spacing $\Delta X' = \Delta x'/h$ from CWG_1. The average wave amplitude attenuation $\beta = 100[(A_1 - A_7)/A_1]$ between CWG_1 and CWG_7 is compared with β_K based on Eq. 2 from Keulegan (subscript K). The product of the wave celerity c_1, determined from the wave centre between CWG_1 and CWG_2, and the wave period T_1 result in the wavelength L_1 (Fig. 3). The discussion of Table 3 follows in the next section both relative to the slide impact zone and the wave attenuation.

5 Discussion of results

5.1 Slide impact zone

The primary reason for scale effects in the slide impact zone between a model and the prototype is a different impact crater formation and air entrainment depending simultaneously on the inertia, the viscosity, and the surface tension (Führböter 1970). The impact crater affects mainly the primary impulse wave generation, whereas the air entrainment rather influences the wave train formation. For both the outward collapsing impact crater (Fritz et al. 2003) and for waves exceeding the stability criteria, the primary wave consists of a massive air–water mixture. Typical impact craters relating to the scale series S6 are shown for S6/1 in Fig. 6a and for S6/2 in Fig. 6b at corresponding relative times. Figure 6b is increased by a factor of 2 for an optical appreciation of the phenomena. The water displacement in Fig. 6a is visibly larger than in Fig. 6b, resulting in a higher wave amplitude at CWG_1.

Figure 7 illustrates the differences of air entrainment and air detrainment at two instants for tests S7/2 and S7/3. Both Figs. 7b and 7d were again increased by a factor of 2. The relative primary wave crest positions in Figs. 7a, b and in c, d are similar. However, wave amplitudes are smaller in Fig. 7b and d than in the corresponding Fig. 7a and c. The amount of air entrained is obviously much larger in test S7/2 than in test S7/3. Despite the air entrainment

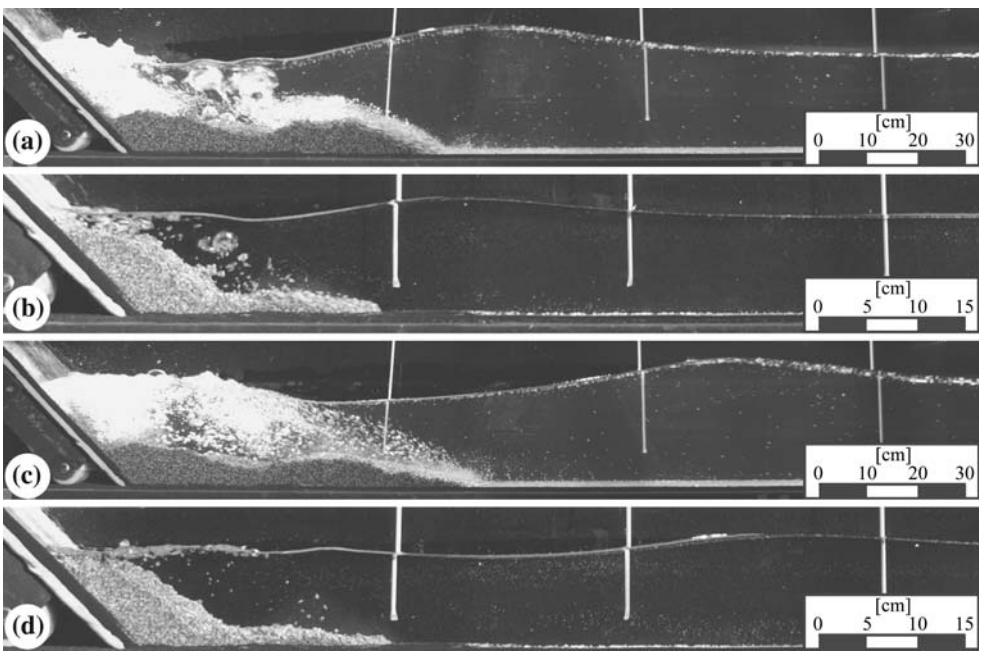

Fig. 7 Comparison of air entrainment and detrainment for S7/2 and S7/3 at similar relative wave crest distances between (**a**) and (**b**), and between (**c**) and (**d**); (**b**) and (**d**) increased by a factor of 2

features differ considerably between these two tests, the energy balance for short turbulent reaches follows the Froude similitude (Le Méhauté 1976, 1990). The effect of surface tension on the primary wave due to air entrainment remains small, because of the immediate wave generation after the slide impact (Fig. 4). However, because the crater formation depends in addition on surface tension (Fig. 6) its effect on the primary wave amplitude is also significant. Accordingly, primary waves without a crater formation are not directly subjected by surface tension. Note that air may in addition be entrained by wave breaking either due to outward collapsing impact craters or at a bore front. The air detraining from the slide impact region lags in time with the slide impact and has no direct influence on the primary wave characteristics. The air detraining effect is not considered in the present research because it focuses the extreme wave features.

The slide deposit shape and the run-out distance are obviously not in similitude, as shown in Fig. 7 (Hampton et al. 1996). The high speed slide impact (F > 1.6) is characterized by phenomena such as sheet flow described by Pugh and Wilson (1999) and depends on the grain size Reynolds number which does not obey the Froude similitude. However, this is again of small relevance for the extreme wave features because the primary wave is generated only by the slide front and has already fully developed prior the slide comes to rest (Fig. 4).

As described previously, it was impossible to keep the dimensionless parameters F, S, and M exactly constant within a scale series (Table 2). Zweifel et al. (2006) (subscript Z) found for the relative maximum wave amplitude with a coefficient of determination 0.92

$$A_M = a_M/h = (1/3)\mathrm{F}S^{1/2}M^{1/4}. \quad (6)$$

The relative amplitude A_1 of Table 3 was identified as the maximum wave amplitude A_M, except for tests S5/1 and S5/2, where it occurred at CWG_2. The relative amplitude difference A_{1dZ} determined from Eq. 6 accounts for the deviations in F, S, and M for a certain test from the reference test parameters within a scale series (Table 3). The scale effect corresponds to the total (subscript *tot*) relative amplitude difference $A_{1dtot} = A_{1d} + A_{1dZ}$.

For the minimum still water depth h = 0.075 m used in the present test program, the amount of −2.9% in A_1 of test S5/3 as compared with test S5/1 appears small. However, the wave profiles of these two tests differ considerably. Further, the relative maximum wave amplitudes A_M were located at CWG_2 (X_M = 8.1) for S5/1 and S5/2 whereas it was at CWG_1 (X_M = 4.77) for S5/3. All relative amplitudes A_1 based on a still water depth h = 0.100 m were at least by 13% smaller than of the reference tests. Experiments conducted with h = 0.150 m were inconsistent. They differed from −55.6% to +13.6% (Table 3). In contrast, the deviations in A_1 of all tests with $h \geq 0.200$ m do not exceed 1.8%, except for test S7/2 conducted with a smaller channel width b. The primary wave characteristics may therefore adequately be retained if the still water depth h has a minimum of 0.200 m. A more general condition will be presented below.

The slide impact velocity V_s was determined with the energy equation applied between the slide release position from the box and the impact location involving the slide centre of gravity and the dynamic bed friction angle δ (Fritz 2002). The slide impact velocity V_s resulting directly from the slide profiles was inaccurate because of individual grains located above the slide body and the water splash formation. Consequently, the effect of the dividing wall used for the narrow test arrangements was not included in V_s and thus its disturbance remained unknown. Therefore series S6 and S7 were excluded from the final data analysis. However, tests S6/1 and S6/2 as shown in Fig. 6, and tests S7/2 and S7/3 in Fig. 7 were compared because both were equally affected by the dividing wall.

According to Fritz (2002) the wave celerity of impulse waves may be approximated with the solitary wave celerity

$$c_1 = [g(h + a_1)]^{1/2}. \quad (7)$$

A wave with a large amplitude a_1 travels faster than does a small wave (Fig. 5). The wave profiles of test S4 plotted previously in Fig. 5B were adapted in Fig. 8 with the adjusted effective relative amplitude η/h by considering A_{1dZ}. The wave celerity c_1 was adjusted with Eq. 7 by accounting for the effective relative amplitude. Test S4/2 matches the primary wave of the reference experiment S4/1 quite well and scale effects are again negligible provided $h \geq 0.200$ m, whereas test S4/3 with h = 0.100 m results

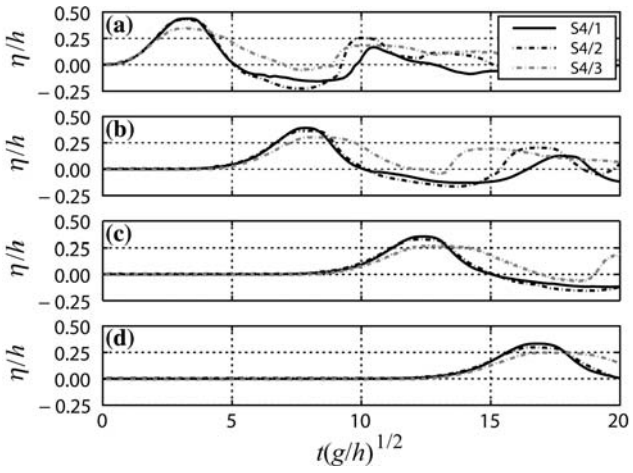

Fig. 8 Adjusted relative wave profiles $\eta/h[t(g/h)^{1/2}]$ with Eqs. 6 and 7, respectively, for scale series S4 at locations (**a**) CWG_1, (**b**) CWG_3, (**c**) CWG_5, and (**d**) CWG_7

in considerable scale effects. The wave train behind the primary wave of Fig. 8 for S4/2 is less accurate than in Fig. 5B. The corrections based on Eqs. 6 and 7 apply only for the relative maximum wave amplitude A_M, whereas the wave profiles of Fig. 8 including troughs were adjusted according to A_{1dZ} of Table 3. Note that the CWGs measure a pure water column and may be influenced by air presence in the wave train. The relative grain diameter D_g was demonstrated to have a small effect on the primary wave amplitude a (Heller 2007a). Because the primary wave crest has normally the highest amplitude in subaerial landslide generated impulse waves (Zweifel et al. 2006), wave trains are often of secondary relevance in engineering applications. No additional analysis on these aspects was therefore made herein. Generalized criteria for impulse waves experimentation without scale effects are presented below.

5.2 Wave attenuation

The parameter L_1/h of Table 3 allows for a wave classification into deep ($L_1/h < 2$), intermediate ($2 \leq L_1/h \leq 20$), and shallow ($L_1/h > 20$) water waves (Le Méhauté 1976). Therefore, all conducted tests relate to intermediate-water waves. The wave amplitude attenuation for a laminar flow may be predicted with Eq. 1. The smallest wavelength $L_1 = 0.70$ m relates to test S1/3 (Table 3). To reduce the wave amplitude by 1% Eq. 1 requires a propagation time $t = 65$ s, whereas the primary model impulse wave travelled the distance of $\Delta x' = 1.5$ m with the wave celerity $c_1 = 1.07$ m/s in only 1.4 s (Tables 2, 3). Therefore, the wave amplitude attenuation due to internal friction is negligible (Biesel 1949; Fritz 2002), even if the wave profiles of the present research differ from sinusoidal waves. The wave amplitude attenuation due to boundary layer effects based on Eq. 2 is expressed with β_K in Table 3. It is by a factor of 6 up to 73 too small to explain the measured wave amplitude attenuation β. The reason for this discrepancy may be a combination of three components: (1) the generated impulse waves differ from the ideal solitary wave profile (Fig. 5); (2) Eqs. 1 and 2 include only the turbulent boundary layer, but no air entrainment and turbulence in the water body (Biesel 1949); and (3) frequency dispersion affects the investigated intermediate-water waves (Dean and Dalrymple 2004). It remains unknown which of these three components dominates. No detailed frequency dispersion analysis was conducted because it was out of the scope of the present study and because of the limited channel length. However, Panizzo et al. (2002) showed that frequency dispersion plays an important role in landslide generated impulse waves. No obvious trend of β may be observed in Table 3 within a scale series. Tests S1 and S2 with a small relative amplitude A_1 tend to a larger amplitude attenuation β, except for S6. This may be explained with the different wave types observed (Huber 1980; Heller 2007a).

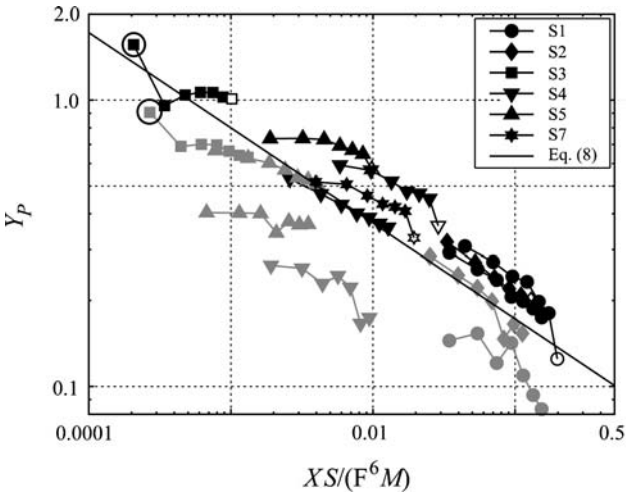

Fig. 9 Relative primary wave height $Y_P = H_P/h$ versus $XS/(F^6M)$; *black symbols* refer to tests with negligible scale effects and *grey* to tests with a considerable scale effect; *circled data* are influenced by the *splash* and *open data* by wave reflection

Figure 9 shows the relative primary wave height $Y_P = H_P/h$ versus the parameter $XS/(F^6M)$. All tests with channel width $b = 0.500$ m were considered. Tests with negligible scale effects are marked in black and those with a considerable scale effect in grey. The scale series S3 resulted in an outward collapsing impact crater according to Fritz et al. (2003) due to a large Froude number F (Table 2). This crater and the produced splash caused recording problems at CWG_1 and the related data are circled in Fig. 9. The open symbols are influenced by wave reflection from the channel end. A separation of tests into those with and without scale effects is possible with

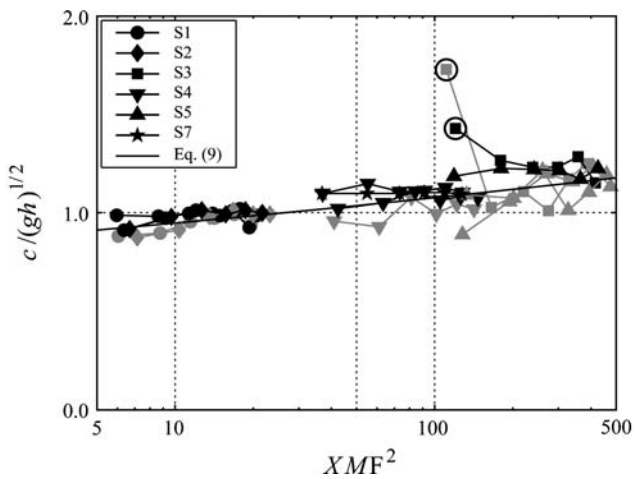

Fig. 10 Relative primary wave celerity $c/(gh)^{1/2}$ versus XMF^2; notation see Fig. 9

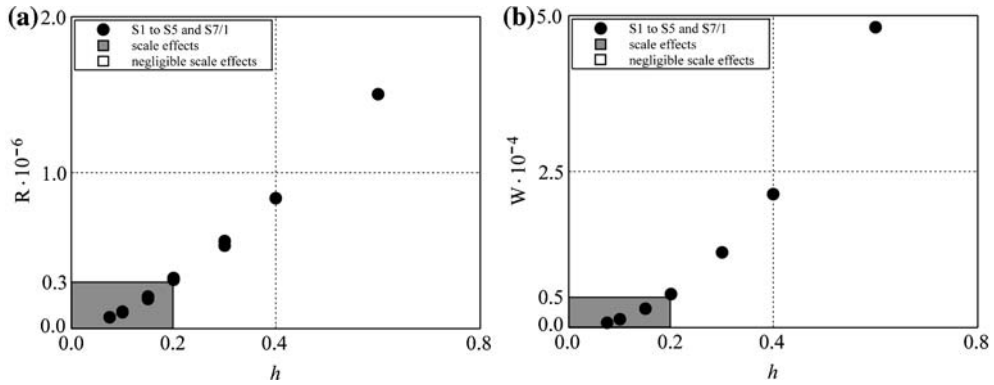

Fig. 11 Region of scale effects (*grey*) for wave tests with water and air, still water depth h versus (**a**) Reynolds number R from Eq. 3 and (**b**) Weber number W from Eq. 4

$$Y_P = 0.08[XS/(\mathrm{F}^6 M)]^{-1/3}. \quad (8)$$

The relative wave height Y_P of tests with noticeable scale effects is always smaller than that of the remainder. In general, scale effects lead to a larger damping than do tests without scale effects as a consequence of mainly fluid viscosity.

Figure 10 shows the relative wave celerity $c/(gh)^{1/2}$ between CWG_1 and CWG_2 (Table 3) versus the parameter $XM\mathrm{F}^2$. The tests with and without scale effects may be separated with

$$c/(gh)^{1/2} = (5/6)(XM\mathrm{F}^2)^{1/18}. \quad (9)$$

Impulse waves with a considerably scale effect are slower than the reference tests. Surface tension effects have no major influence on the wave celerity in pure water if $T \geq 0.35$ s and $h \geq 2$ cm (Le Méhauté 1990; Hughes 1993). Therefore, all tests satisfy these criteria and the change in wave celerity is not due to surface tension (Table 3). Accordingly, wave attenuation is mainly affected by fluid viscosity and frequency dispersion. The wave celerity depends on the wave amplitude a (Eq. 7). Waves with a large wave height have in general larger wave amplitudes and travel faster than do waves with a smaller wave height. The differences of wave celerities for tests with and without scale effects is attributed to the differences in the wave height, as shown in Fig. 9; therefore Fig. 10 allows to assess the relative importance of the governing parameters for negligible scale effects. Note that the wave celerity is less sensitive to scale effects as compared with the wave height (Fig. 9).

5.3 Limitations for scale effects

Impulse waves may be investigated experimentally using the Froude similitude provided scale effects are small. The present research aimed to investigate the effects of surface tension and fluid viscosity on families of carefully planned impulse wave series. Herein, the primary wave height and the wave celerity were the main parameters investigated. Further attention was directed to the wave crater formation and air entrainment and detrainment.

Limitations for impulse wave modelling using the Froude law of similitude include limits for the Reynolds and the Weber numbers, as defined in Eqs. 3 and 4. From Sects. 5.1 and 5.2 identical limit Weber W_L and Reynolds R_L numbers apply for both wave attenuation and wave generation. The data analysis results in a limit (subscript L) Reynolds number of $\mathrm{R}_L = g^{1/2}h_L^{3/2}/\nu_w = 3\times10^5$ and a limit Weber number of $\mathrm{W}_L = \rho_w g h_L^2/\sigma_w = 5{,}000$ (Table 3). The involved fluids are water and air and the governing dimensionless parameters are in the range of $1.68 \leq \mathrm{F} \leq 4.25$, $0.15 \leq S \leq 0.53$, and $0.54 \leq M \leq 2.24$.

Figure 11 illustrates the resulting domain of scale effects and the test conditions of Table 2 except for tests S6/1, S6/2, S7/2, and S7/3 with a smaller channel width b than used for the main tests. The still water depth h versus the Reynolds number R is shown in Fig. 11a, whereas Fig. 11b relates to the Weber number W. In the shaded zone scale effects are at least 1.8% based on the relative wave amplitude A_1. The limit Reynolds number $\mathrm{R}_L = 3 \times 10^5$ and the limit Weber number $\mathrm{W}_L = 5{,}000$ conform to a limit still water depth $h_L = 0.200$ m in a 0.5 m wide wave channel.

6 Conclusions

Scale effects in subaerial landslide generated impulse waves based on the Froude similitude may considerably affect the results if applying too small model dimensions. Scale effects arise mainly as a consequence of surface tension and fluid viscosity. The three phases involved in these flows are solid,

water, and air. A dimensional analysis resulted in five dimensionless parameters; these were held constant within seven selected scale series to analyse scale effects. All generated impulse waves were in the intermediate-wave regime. Scale effects reduce the relative wave amplitude whereas their effect on the wave celerity was found to be relatively small. The impact crater formation was attributed to be the primary and obvious reason for scale effects due to surface tension. The air transport affects in addition the wave train formation. Viscosity and frequency dispersion may have a significant effect on the impulse wave height attenuation which exceeds available analytical results for solitary waves by up to a factor of 73. The presence of air was found to be responsible for scale effects in the wave generation zone, whereas viscosity has the main effect in the wave propagation zone. The limiting criteria for modelling subaerial landslide generated impulse waves presented in Sect. 5.3 are consistent with related coastal engineering studies.

Acknowledgments The first author was supported from the Swiss National Science Foundation, Grant 200020-103480/1.

References

Abelson HI (1970) Pressure measurements in the water-entry cavity. J Fluid Mech 44(1):129–144

Biesel F (1949) Calcul de l'amortissement d'une houle dans un liquide visqueux de profondeur finite (in French). La Houille Blanche 4(5):630–634

Buckingham E (1914) On physically similar systems. Phys Rev 4:354–376

De St Q Isaacson M (1976) The viscous damping of cnoidal waves. J Fluid Mech 75(3):449–457

Dean RG, Dalrymple RA (2004) Water wave mechanics for engineers and scientists: advanced series on ocean engineering, vol 2. World Scientific, Singapore

Fritz HM (2002) Initial phase of landslide generated impulse waves. In: Minor H-E (ed) VAW-Mitteilung, vol 178. Versuchsanstalt für Wasserbau, Hydrologie und Glaziologie, ETH, Zurich

Fritz HM, Moser P (2003) Pneumatic landslide generator. Int J Fluid Power 4(1):49–57

Fritz HM, Hager WH, Minor H-E (2001) Lituya bay case: rockslide impact and wave run-up. Sci Tsunami Hazards 19(1):3–22

Fritz HM, Hager WH, Minor H-E (2003) Landslide generated impulse waves. Exp Fluids 35:505–532 doi:10.1007/s00348-003-0659-0

Führböter A (1970) Air entrainment and energy dissipation in breakers. In: Proceedings of the 12th coastal engineering conference, Washington DC, vol 1. ASCE, New York, pp 391–398

Hager WH, Bremen R (1989) Classical hydraulic jump: sequent depths. J Hydraul Res 27(5):565–585

Hampton MA, Lee HJ, Locat J (1996) Submarine landslides. Rev Geophys 34(1):33–59

Heinrich P (1992) Nonlinear water waves generated by submarine and aerial landslides. J Waterw Port Coast Ocean Eng 118(3):249–266

Heller V (2007a) Landslide generated impulse waves: prediction of near field characteristics. Dissertation 17531, ETH, Zurich (submitted)

Heller V (2007b) Massstabseffekte im hydraulischen Modell (in German). Wasser Energie Luft 99(2):153–159

Huber A (1976) Grenzen der Froude'schen Ähnlichkeit bei der Nachbildung flacher Wasserwellen im hydraulischen Modell (in German). In: Vischer D (ed) VAW-Mitteilung, vol 21. Versuchsanstalt für Wasserbau, Hydrologie und Glaziologie, ETH, Zurich

Huber A (1980) Schwallwellen in Seen als Folge von Bergstürzen (in German). In: Vischer D (ed) VAW-Mitteilung, vol 47. Versuchsanstalt für Wasserbau, Hydrologie und Glaziologie, ETH, Zurich

Hudson RY, Herrmann FA, Sager RA, Whalin RW, Keulegan GH, Chatham CE, Hales LZ (1979) Coastal hydraulic models. Special report no 5, US Army Engineer Waterways Experiment Station, Vicksburg, Mississippi

Hughes S (1993) Physical models and laboratory techniques in coastal engineering. Advanced series on ocean engineering, vol 7. World Scientific, Singapore

Ippen AT, Kulin G (1957) The effects of boundary resistance on the solitary wave. La Houille Blanche 12(3):390–407

Iwasa Y (1959) Attenuation of solitary waves on a smooth bed. Trans ASCE 124:193–206

Kamphuis JW, Bowering RJ (1972) Impulse waves generated by landslides. In: Proceedings of 12th Coastal Engineering Conference, Washington DC, vol 1. ASCE, New York, pp 575–588

Keulegan GH (1950) Wave motion. In: Rouse H (ed) Engineering hydraulics. Wiley, New York

Le Méhauté B (1976) An introduction to hydrodynamics and water waves. Springer, New York

Le Méhauté B (1990) Similitude. In: Le Méhauté B, Hanes DM (eds) The sea ocean engineering science, vol 9B. Wiley, New York, pp 955–980

Miles JW (1976) Damping of weakly nonlinear shallow-water waves. J Fluid Mech 76(2):251–257

Miller DJ (1960) Giant waves in Lituya Bay, Alaska. Geological survey, Professional paper 354-C. US Government Printing Office, Washington DC

Miller RL (1972) The role of surface tension in breaking waves. In: Proceedings of the 13th coastal engineering conference, Vancouver BC, vol 1. ASCE, New York, pp 433–449

Noda E (1970) Water waves generated by landslides. J Waterw Harb Coast Eng Div ASCE 96(WW4):835–855

Panizzo A (2004) Physical and numerical modelling of subaerial landslide generated waves. Dissertation, Università degli studi, L'Aquila, Italy

Panizzo A, De Girolamo P (2005) Forecasting impulse waves generated by subaerial landslides. J Geophys Res 110(C12025):1–23 doi: 10.1029/2004JC002778

Panizzo A, Bellotti G, De Girolamo P (2002) Application of wavelet transform analysis to landslide generated waves. Coast Eng 44:321–338

Pugh FJ, Wilson KC (1999) Velocity and concentration distributions in sheet flow above plane beds. J Hydraul Eng 125(2):117–125

Skladnev MF, Popov IY (1969) Studies of wave loads on concrete slope protections of earth dams. In: Research on wave action, vol 2(7). Delft, The Netherlands, pp 1–11

Stive MJF (1985) A scale comparison of waves breaking on a beach. Coast Eng 9:151–158

Treloar PD, Brebner A (1970) Energy losses under wave action. In: Proceedings of the 12th coastal engineering conference, Washington DC, vol 1. ASCE, New York, pp 257–267

Walder JS, Watts P, Sorensen OE, Janssen K (2003) Tsunami generated by subaerial mass flows. J Geophys Res 108(B5):2.1–2.19

Zweifel A, Hager WH, Minor H-E (2006) Plane impulse waves in reservoirs. J Waterway Port Coast Ocean Eng 132(5):358–368